Journal of Materials Chemistry A

ROYAL SOCIETY OF CHEMISTRY

PAPER

View Article Online
View Journal

Cite this: DOI: 10.1039/d5ta09547f

Tensile strain engineering on Cu nano-dots for high efficiency HMFOR at low potential

Honglei Chen,[a] Yanming Li,[a] Wenbin Ma,[a] Qi Chen,[a] Xupeng Qin,[b] Yitao Liu,[a] Lan Wang,[ac] Qinghua Liu,[b] Chunzhen Yang,*[a] Changli Li*[a] and Jingfu He*[a]

Received 24th November 2025
Accepted 8th March 2026

DOI: 10.1039/d5ta09547f

rsc.li/materials-a

The electrochemical conversion of biomass is a promising route to sustainable fuels and chemical feedstocks but is often limited by sluggish catalyst kinetics at low overpotentials. Here, we demonstrate that tensile strain engineering of Cu can substantially enhance its electrocatalytic activity toward the oxidation of biomass-derived 5-hydroxymethylfurfural (HMF). Transmission electron microscopy (TEM) and pair distribution function (PDF) analyses confirmed that continuous tensile strain (0–6%) was introduced into Cu nanoparticles through electroreduction of copper-iodide precursors. The optimized strained Cu catalyst (ID-Cu, 6% strain) achieved a high current density of ~100 mA cm^{-2} at 0.3 V *vs.* RHE, with nearly 100% selectivity toward 5-hydroxymethyl-2-furancarboxylic acid (HMFCA) and a faradaic efficiency of 99%. *in situ* Raman and FTIR measurements revealed that the adsorption of the key *OCHO intermediate strengthened progressively with increasing strain. Density functional theory (DFT) calculations further showed that tensile strain modulates the Cu d-band center, enhancing the binding energy of *OCHO by 0.9 eV. This work establishes a new paradigm for designing efficient electrocatalysts *via* lattice strain engineering.

Introduction

The electrochemical conversion of biomass holds significant potential in providing green chemical feedstocks and fuels without the need for external energy input, presenting a promising approach to address global energy and environmental challenges.[1–4] The realization of large-scale industrial applications for biomass electrochemical conversion requires systematic optimization of catalyst kinetics under low overpotentials.[5–7] Among various catalysts, copper-based catalysts are currently the only effective ones capable of efficiently catalyzing aldehyde substrates such as 5-hydroxymethylfurfural (HMF), achieving >50 mA cm^{-2} current density at overpotentials of 0.1–0.3 V.[8–11] Although this has reduced the potential by about 1 V compared with the conversion of HMF to high-value products of FDCA at traditional high potential,[12–17] the kinetics remain far from ideal, making fine-tuning of the Cu electronic structure a central challenge in advancing this field.[18]

The catalytic activity of HMF oxidation (HMFOR) is strongly dependent on the regulation of Cu electronic structure. While Cu^0 can adsorb the HMF reactant, both experimental and theoretical studies indicate that the intrinsic binding ability of Cu^0 to OCHO* intermediates is relatively weak compared to the ideal value,[9,10,19,20] requiring assistance from Cu^+ for substrate dissociation. This delicate Cu^0/Cu^+ balance is difficult to control and prone to deactivation under high voltage operating conditions.[21–23] Although tailoring catalyst morphology and nanostructures can tune local valence states to enhance Cu-substrate interactions and activity, such approaches still face significant limitations.[24–26] Conventional morphology control often lacks sufficient tunability and clear correspondence with electronic structure, hindering systematic catalyst optimization.

Strain engineering offers a compelling alternative, as lattice expansion or contraction can quantitatively modulate the metal d-band center and thereby tune substrate binding energies.[27] This approach has been successfully applied in fields such as the oxygen reduction reaction (ORR) and oxygen evolution reaction (OER).[28,29] For instance, it has been reported that nano-alloy of CoRu can introduce tensile lattice for Co, leading to faster interfacial electron transfer kinetics for hydrogen evolution reaction.[30] Core–shell structure can also introduce lattice strain due to the lattice mismatch of core–shell structure, which was applied to P-doped core–shell structure to strengthen the adsorption of OH* and H*.[31] Other methods, such as ligand modification or intercalation in metal–organic frameworks and 2D materials, have also been used to impose strain.[32,33] However, these strategies often rely on ultrasmall

[a]School of Materials, Shenzhen Campus of Sun Yat-sen University, No. 66, Gongchang Road, Guangming District, Shenzhen, Guangdong 518107, P.R. China. E-mail: yangchzh6@mail.sysu.edu.cn; lichli5@mail.sysu.edu.cn; hejf27@mail.sysu.edu.cn
[b]National Synchrotron Radiation Laboratory, University of Science and Technology of China, Hefei 230029, Anhui, P.R. China
[c]School of Chemical Engineering, Sichuan University of Science and Engineering, Zigong 643000, People's Republic of China

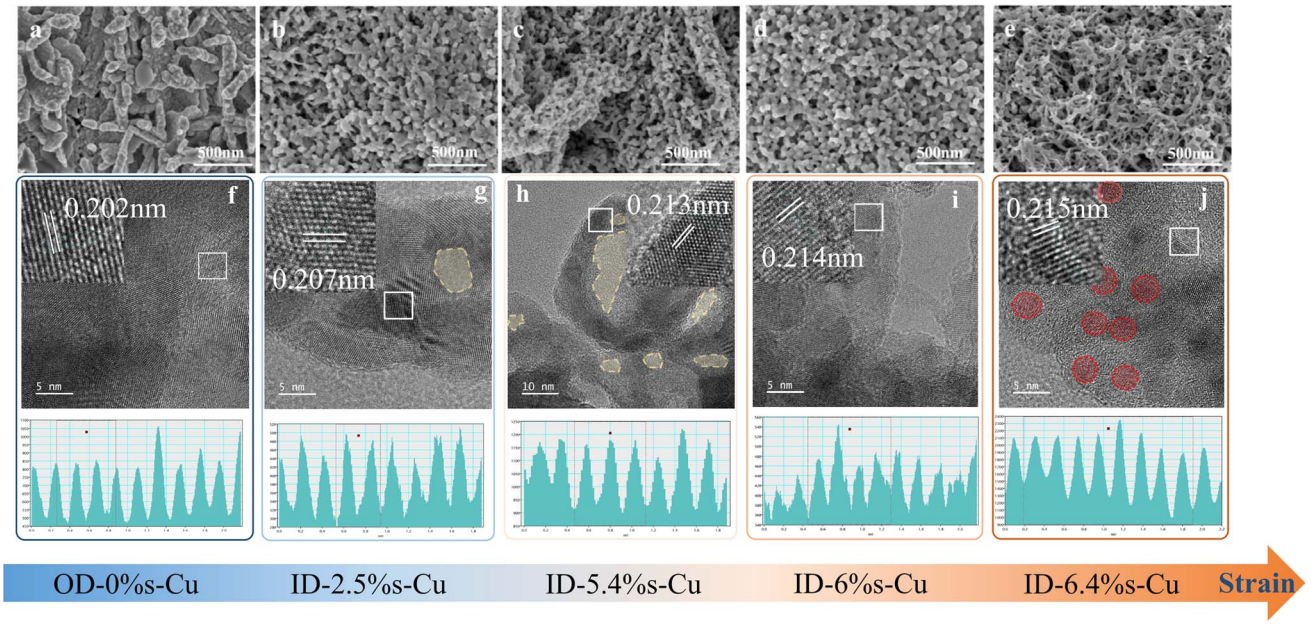

Fig. 1 SEM images of (a) OD-0%s-Cu, (b) ID-2.5%s-Cu, (c) ID-5.4%s-Cu, (d) ID-6%s-Cu and (e) ID-6.4%s-Cu. HRTEM images of the (111) plane of the (f) OD-0%s-Cu, (g) ID-2.5%s-Cu, (h) ID-5.4%s-Cu, (i) ID-6%s-Cu and (j) ID-6.4%s-Cu, respectively.

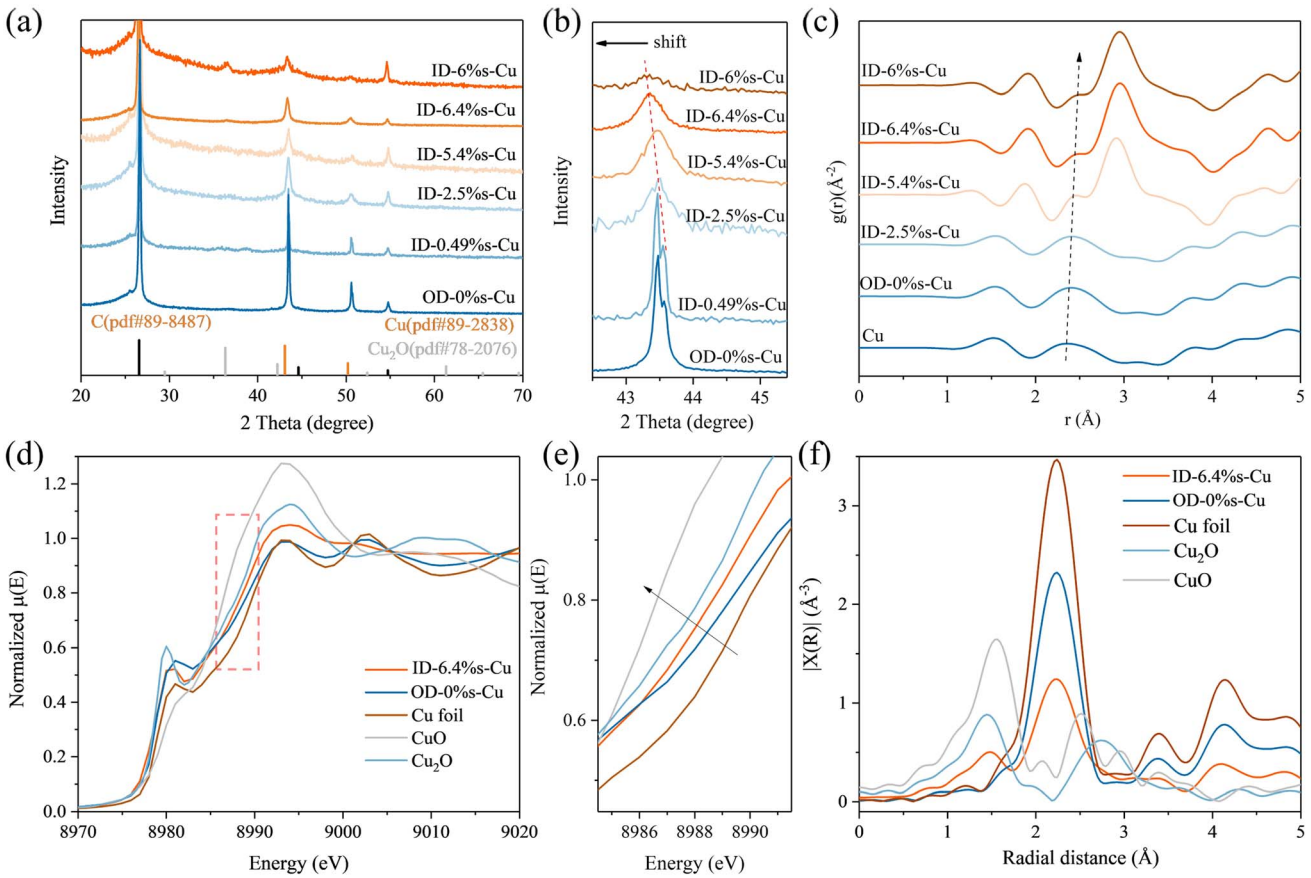

Fig. 2 (a and b) XRD patterns of OD-0%s-Cu, ID-0.49%s-Cu, ID-2.5%s-Cu, ID-5.4%s-Cu, ID-6%s-Cu and ID-6.4%s-Cu. (c) Pair distribution function (PDF) data of OD-0%s-Cu, ID-2.5%s-Cu, ID-5.4%s-Cu, ID-6%s-Cu and ID-6.4%s-Cu. (d and e) Cu K-edge XANES spectra of ID-6.4%s-Cu, BD-Cu, CD-Cu, OD-0%s-Cu, Cu foil, CuO and Cu_2O. (f) Corresponding FT EXAFS spectra of ID-6.4%s-Cu, BD-Cu, CD-Cu, OD-0%s-Cu, Cu foil, CuO and Cu_2O.

nanostructures that deactivate under harsh conditions or introduce foreign elements that disrupt intrinsic activity.[34–36] Thus, there is a critical need to design robust schemes that can stably and quantitatively introduce strain in Cu without compromising its intrinsic surface activity toward HMFOR, to systematically analyze the relationship between the d-state electronic structure and catalytic performance.

In this work, we report a halogenation–electroreduction strategy to introduce controllable tensile strain into nanostructured Cu. Complete iodination of Cu, followed by reduction, produced small Cu nanocrystals encircled in Cu_2O, where interfacial lattice mismatch generated tensile strain. Characterization by TEM, PDF, and XAFS confirmed the presence of strain from 0.4% to 6.4%, which correlated directly with enhanced catalytic activity: strained Cu achieved a current density of 100 mA cm^{-2} at 0.3 V *vs.* RHE with nearly 100% HMFCA selectivity. *In situ* Raman and IR spectroscopy showed progressively stronger *OCHO adsorption with increasing strain, while DFT calculations revealed that tensile strain raises the Cu d-band center, strengthening *OCHO binding and accelerating the rate-limiting step of HMF conversion. This study demonstrates a robust and tunable strategy for strain engineering, providing mechanistic insights into how lattice strain governs Cu's electronic structure and catalytic performance in biomass electrooxidation.

Results and discussions

We employed a two-step synthesis to prepare strain-engineered Cu catalysts *via* controlled halogenation followed by electrochemical reduction. In the first step, metallic Cu substrates were iodinated for varying durations (1–60 min). Subsequent electrochemical reduction effectively converted the iodinated layers back to metallic copper, producing a series of iodide-derived copper samples, designated as ID-*x*%s-Cu (x = measured strain). For comparison, hydroxylation-, chlorination-, and bromination-derived Cu catalysts were also synthesized, designated as OD-Cu, CD-Cu, and BD-Cu.

SEM images revealed that the halogen species strongly influenced the resulting morphologies (Fig. 1 and S1–5).[37–39] CuI samples exhibited characteristic micro-sheet structures with crystal size increasing with iodination time. CuOH, CuCl and CuBr samples have micro-wire, micro-particle and micro-cone morphologies, respectively (Fig. S1–5). After electrochemical reduction, the corresponding OD-Cu, CD-Cu, and BD-Cu samples transformed into nanocolumns, nanocubes, and nanoparticles, respectively. Notably, ID-Cu samples exhibited nanoparticle morphologies with reduced crystallite sizes and porous features. ICP test exhibits that the residual amount of halogen ions is 1–2%, indicating nearly complete reduction of copper halides during post-treatment.

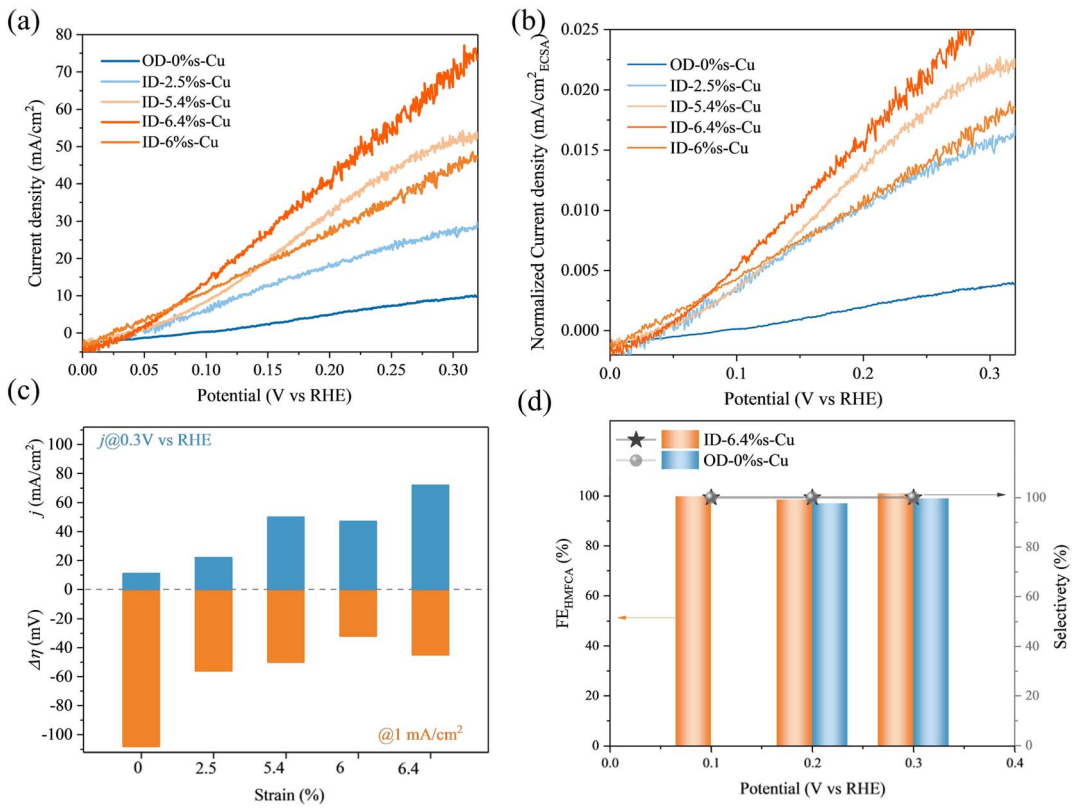

Fig. 3 Electrochemical performance of Cu catalysts with various strain degrees. (a) LSV curves and (b) ECSA-normalized LSV curves of OD-0%s-Cu and ID-*x*%s-Cu, whose strain degree (x) is 2.4%, 5.4%, 6.4% and 6% in an electrolyte containing 1 M KOH and 50 mM HMF. (c) $\Delta\eta$ at 1 mA cm^{-2} and j at 0.3 V *vs.* RHE of OD-0%s-Cu and ID-*x*%s-Cu. (d) FE of HMFCA and selectivity for OD-0%s-Cu and ID-6.4%s-Cu under various potential in an electrolyte containing 1 M KOH and 50 mM HMF.

High-resolution TEM (HRTEM) further revealed that iodination duration directly influenced lattice parameters, with OD-Cu as reference. It is worth noting that with the increase in iodination time, the Cu crystalline domains obtained after reduction become significantly smaller, which is consistent with the reduction in particle size observed in SEM results. The HRTEM image in Fig. 1f shows a lattice parameter of 2.02 Å in the OD-Cu nanocolumn, consistent with unstrained Cu (111) planes. By contrast, ID-Cu samples displayed progressively larger lattice spacings with increased iodination time, expanding from 2.03 Å (iodination for 1 min) to 2.15 Å (iodination for 30 min), corresponding to tensile strains up to 6.4% (Fig. 1g–j and S6). The successful introduction of lattice strain could be further confirmed by the X-ray diffraction (XRD) patterns as shown in Fig. 2 and S9. As shown in Fig. 2a, with the increase of iodination time, the Cu (111) crystal plane at 43.3° becomes broader, indicating that iodination hindered the crystalline process of Cu during electrochemical reduction (Fig. 2b). The position of Cu (111) crystal plane shift from 43.5° to 43.1°with the prolonged iodination time, confirming the introduction of tensile strain, which is the same trend like TEM calculated by Bragg equation.[40,41]

Pair distribution function (PDF) analysis further validated the Cu–Cu bond elongation in ID-Cu samples (Fig. 2c and S11). It can be clearly seen that the pure Cu has the Cu–Cu bond of 2.3 Å, the Cu–Cu bond value of OD-0%s-Cu is same as pure Cu, illustrating the same structure of single Cu of OD-0%s-Cu. As the degree of iodination increases, the tensile degree of Cu lattice is enhanced, resulting in the Cu–Cu bond of ID-6.4%s-Cu increased to 2.5 Å compared to the 2.35 Å of ID-2.5%s-Cu. Another important difference is that the Cu–O bond is evident in the ID-Cu samples. During electrochemical reduction, copper halide is nearly completely consumed. Therefore, the Cu_2O in the ID-Cu sample most likely formed from natural oxidation in air or water, facilitated by the small grain boundaries of the Cu. This difficulty in achieving large Cu particles is likely due to an increase in lattice defects caused by I-doping. Combined with the TEM images, it can be found that the longer the iodination time, the smaller the Cu grains wrapped in Cu_2O, and the Cu–Cu bond length gradually changes from 2.3 Å to 2.5 Å. The Cu valence state is evaluated based on the position of the absorption edge in the Cu K-edge X-ray absorption near-edge structure (XANES) spectroscopy (Fig. 2d–f and S12).[42,43] The absorption edge position of compound derived Cu follows the order of Cu_2O > ID-Cu > BD-Cu > CD-Cu > OD-Cu > Cu foil, consistent with the observation that Cu crystalline is encircled in Cu_2O. Further fitting of extended X-ray absorption fine structure (EXAFS) result for ID-Cu shows that the Cu–Cu bond length is increased by 0.2% compared with that of the standard metal Cu, and there is an obvious disorder. This

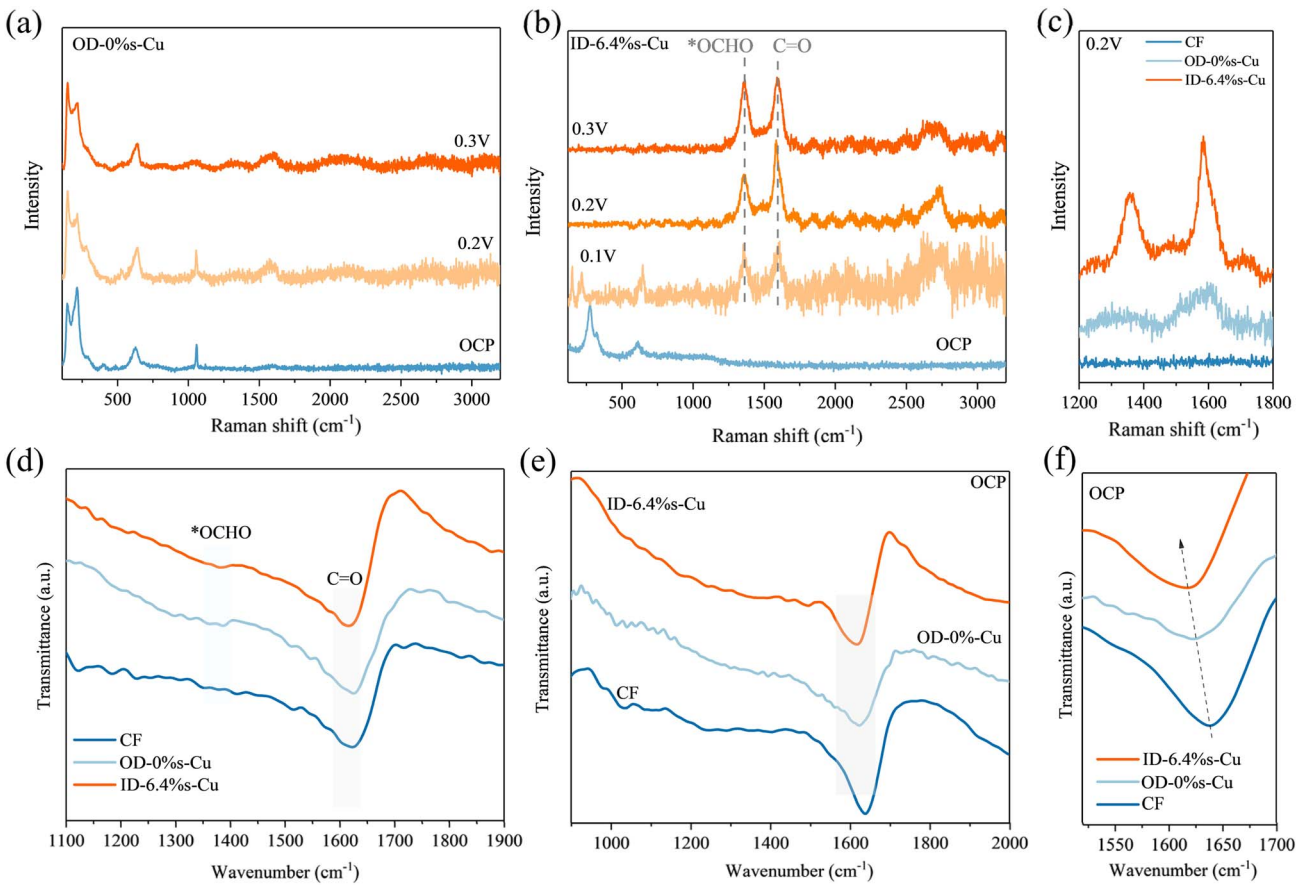

Fig. 4 *In situ* Raman spectra in an electrolyte of 1.0 M KOH and 0.05 M HMF solution at different voltages of (a) OD-0%s-Cu, (b) ID-6.4%s-Cu and (c) enlarged *in situ* Raman spectra. *In situ* FTIR spectra of CF, ID-6.4%s-Cu and OD-0%s-Cu in an electrolyte of 1.0 M KOH and 0.05 M HMF solution at (d) 0.3 V and (e) OCP. (f) Enlarged *in situ* FTIR spectra.

is consistent with the hypothesis that the tensile stress stems from the Cu_2O/Cu interfacial mismatch, as evidenced by our Raman and XPS data (Fig. S13 and 14). As shown in Fig. S13(a–d), the Cu–I, Cu–Br, Cu–Cl bond present at 125 cm^{-1}, 176 cm^{-1} and 230 cm^{-1}, respectively.[44–47] After electro-reduction, OD-Cu, ID-Cu, BD-Cu and CD-Cu show the characteristics of Cu–O bond.[48] With the increase of lattice tensile strain of Cu, the mode of Cu–O bond (280 cm^{-1}) is gradually dominated, which corresponds to the unsaturated Cu coordination.

Performance

The impact of tensile strain on HMF oxidation (HMFOR) was evaluated in 1 M KOH electrolyte with 50 mM HMF using an H-cell configuration. Strained Cu catalysts exhibited significantly improved activity compared to strain-free Cu. The onset potential decreased from 0.12 V (OD-Cu) to 0.02 V (ID-6.4%s-Cu), and the current density at 0.3 V_{RHE} reached 70–100 mA cm^{-2} depending on strain level (Fig. 3a–c). Among all samples, ID-6.4%s-Cu delivered the best performance, achieving an overpotential of only 44 mV at 1 mA cm^{-2}, outperforming OD-Cu (110 mV) and moderately strained samples (55–50 mV).

To clarify the intrinsic activity of different catalyst configurations, we measured the electrochemical active areas (ECSA) of each catalyst (Fig. S8). The results show that the relative ECSA values of ID-2.4%s-Cu, ID-5.4%s-Cu, ID-6%s-Cu, and ID-6.4%s-Cu compared to the OD-0%s-Cu sample are 70, 95.2, 102, 104 and 101, respectively. After normalizing for specific surface area factors (Fig. 3b), the catalytic current density of Cu still exhibited a strong positive correlation with strain. The current density per unit area of ID-6.4%s-Cu reached 0.02 mA cm^{-2}@0.2 V, which is five times higher than that of the OD-0%s-Cu sample. Importantly, all Cu-based catalysts achieved nearly 100% selectivity toward HMFCA with faradaic efficiencies of ~99% across the potential range of 0.1–0.3 V_{RHE} (Fig. 3d and S10). It should be noted that OD-0%s-Cu only measures the potential of 0.2–0.3 V_{RHE}, because the potential of 0.1 V_{RHE} cannot provide the positive current of catalytic activity of HMFOR (as shown in Fig. 3a).

To probe the reaction mechanism, *in situ* Raman and FTIR spectroscopy were performed (Fig. 4, S15 and 16). Under the OCP condition, no significant Raman signals were observed for any Cu sample in the frequency range of 1200–2000 cm^{-1}. Upon applying potentials of 0.1–0.3 V, distinct bands at 1300–1400 cm^{-1} appeared, corresponding to the O–C–O symmetric stretching of the *OCHO intermediate,[49,50] which is usually considered as a key HMFOR intermediate for the reaction pathway *via* gem-diol ion,[51,52] while bands at 1520–1600 cm^{-1} were assigned to C=O and C=C vibrations of the furan ring (Fig. 4a–c).[53,54] The intensity of the *OCHO band increased with tensile strain, following the order ID-6.4%s Cu > OD-Cu > Cu, indicating that strain promoted accumulation of *OCHO intermediates (Fig. 4c). In addition, the peak strength of C=O peak presents a similar trend to *OCHO, illustrating a strong adsorption capacity for substrates as strain stretching.

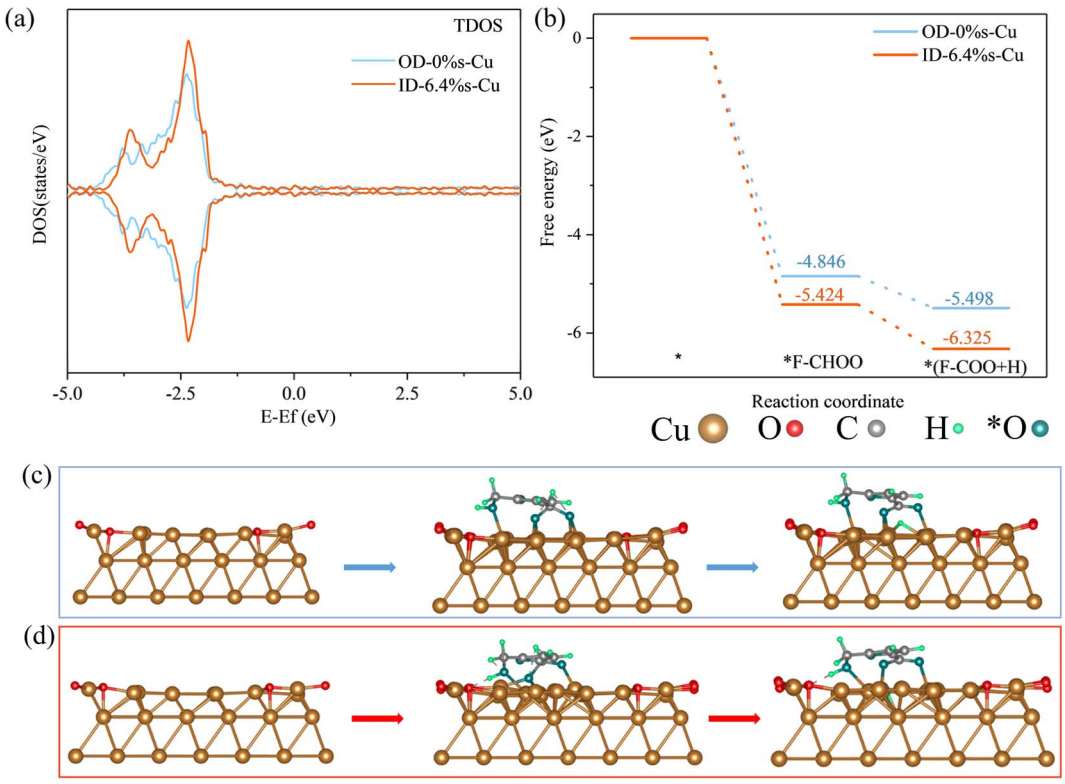

Fig. 5 Theoretical determination of the essential HMF oxidation reaction pathway. (a) Calculated density of states of OD-0%s-Cu and ID-6.4%s-Cu with respect to the Fermi level. (b) Free energy profiles of HMFOR on OD-0%s-Cu and ID-6.4%s-Cu on Cu(111) surface. The reaction pathway of HMFOR on (c) OD-0%s-Cu and (d) ID-6.4%s-Cu based on DFT calculation.

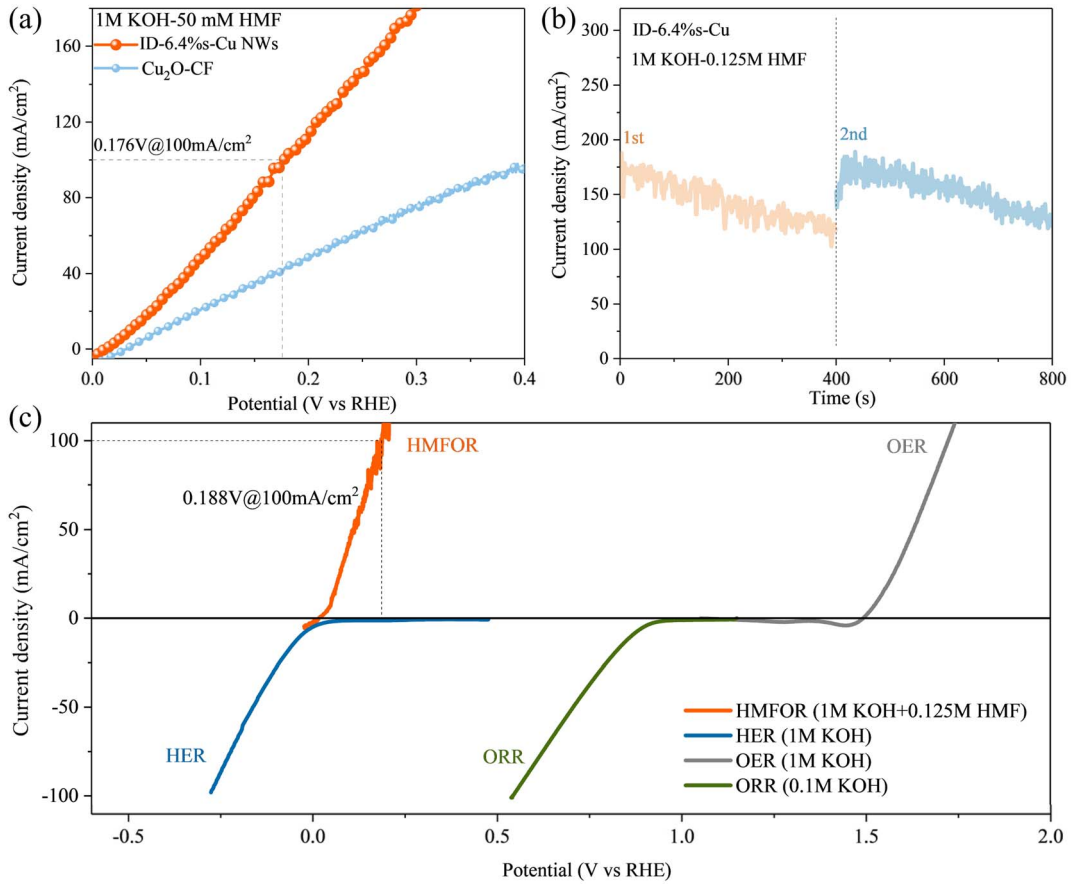

Fig. 6 (a) LSV curves and of ID-6.4%s-Cu NWs and Cu_2O-CF. (b) Stability test of ID-6.4%s-Cu in 1 M KOH and 0.125 M HMF. (c) LSV curves of ORR in 0.1 M KOH by Fe single atom for Zn-air battery, HER in 1 M KOH by Pt foil, OER in 1 M KOH and HMFOR in 1 M KOH with 0.125 M HMF by ID-6.5%s-Cu.

Similarly, *in situ* FTIR spectra confirmed enhanced *OCHO adsorption on strained Cu (Fig. 4d–f). The peak at 1350–1400 cm^{-1} can be assigned to *OCHO, which is evidence for ID-Cu and OD-Cu during operation, showing a rapid transfer from HMF to *OCHO. The peak at 1600–1650 cm^{-1} is related to the C=O stretching of the furan ring,[55,56] which can be observed at OCP, indicating the intrinsic adsorption intensity of HMF on catalysts. In OCP state, Cu foam cannot effectively adsorb HMF, so there is no C=O stretching in Fig. 4f. However, obvious C=O adsorption peaks could be detected for ID-Cu, OD-Cu, and they moved to negative with the strain stretching, which indicated that the introduction of strain effectively reduced the adsorption potential barrier of HMF.

Next, we conducted density functional theory (DFT) calculations to analyze the influence of tensile strain on catalytic activity (Fig. 5 and S17). As shown in Fig. 5a, interaction between adjacent Cu atoms decreases with the tensile strain, leading to the narrowing of d-band and upshift of d-band center. According to the d-band theory, the enhanced d-band center can improve the adsorption capability of Cu catalyst for substrates.[57,58] HMF is unstable in alkaline solution, it absorbs hydroxyl to become gem diol rapidly, and then removes OH^- to become HMFCA and produces H_2 at the same time.[54] Previous research indicates that C–H bond cleavage is the rate-limiting step (RDS) of HMF conversion to HMFCA on the catalyst surface, and the binding strength of HMF on Cu^0 is considered to be weaker than optimal value.[19,20] As the result of tensile strain, ID-6.4%s-Cu sample exhibited a much stronger binding energy between Cu and substrate than that of the OD-0%s-Cu sample, consistent with the improved catalytic kinetics observed experimentally.

Therefore, we designed an alternative approach to modulate the substrate binding energy at Cu active sites *via* strain engineering. The (111) exposed facets of Cu and Cu_2O possess similar atomic arrangements but differ in lattice constant by 16%. By utilizing residual I^- from the CuI precursor to suppress Cu domain growth during reduction, we achieved small-sized Cu nanocrystals. Encapsulated by Cu_2O, these nanocrystals develop tensile strain within the Cu lattice due to interfacial lattice mismatch, reaching a maximum lattice strain of 6.4%. Compared with conventional core–shell structure and intercalation method, our strain engineering method can realize controllable strain and maintain the intrinsic activity of Cu.

By applying this strategy to the best electrode Cu nanowires (Cu NWs) from our previous work can obtain CuI-E-CF NWs with large roughness. CuI-E-CF NWs exhibits ultra-high activities and the current density is as high as 180 mA cm^{-2} at 0.3 V_{RHE} while there is only 70 mA cm^{-2} for Cu_2O/CF (Fig. 6a). Performance tests for low-potential HMF oxidation clearly

demonstrate that the 6% strained Cu catalyst exhibits a two-fold increase in TOF compared to the strain-free Cu catalyst. Besides, ID-6.4%s-Cu with tensile strain has excellent stability (Fig. 6b). Comparing the low potential HMFOR with OER and HER, it can be found that the voltage input of HMFOR and HER paired system is more than 1.5 V less than that of traditional water splitting. Moreover, the low initial potential and strong dynamic characteristics of low potential HMFOR enable it to form a new fuel cell with ORR (Fig. 6c). Therefore, strain engineering samples with good morphology have strong dynamic advantages and show excellent application prospects.

Conclusions

In this work, we demonstrated a generalizable halogenation–reduction strategy to introduce controllable tensile strain in Cu catalysts, enabling highly efficient electrooxidation of HMF to HMFCA. By utilizing residual I^- from the CuI precursor to suppress Cu domain growth during reduction, we achieved small-sized Cu nanocrystals. Encapsulated by Cu_2O, these nanocrystals develop tensile strain within the Cu lattice due to interfacial lattice mismatch, reaching a maximum lattice strain of 6.4%, confirmed by XAFs, TEM, and PDF. The strained Cu catalysts exhibited markedly enhanced activity, with an overpotential as low as 44 mV at 1 mA cm^{-2}, and nearly 100% faradaic efficiency. The concept was successfully extended to Cu nanowires, achieving industrially relevant current densities (180 mA cm^{-2} at 0.3 V) with excellent durability. *In situ* Raman and FTIR spectroscopy reveals that highly strained Cu nanocrystals significantly enhance HMF binding strength, overcoming the widely recognized drawback of weak HMF binding on conventional Cu catalysts. DFT calculations further revealed that strain-induced d-band upshifts strengthened intermediate binding and lowered the C–H bond cleavage barrier. In summary, this study provides fundamental insights into strain-mediated electronic tuning and establishes a versatile approach for designing next-generation Cu-based catalysts for biomass valorization and sustainable energy conversion.

Conflicts of interest

There are no conflicts to declare.

Data availability

The authors confirm that the data supporting the findings of this study are available within the article and/or its supplementary information (SI). Supplementary information is available. See DOI: https://doi.org/10.1039/d5ta09547f.

Acknowledgements

This work was supported by the Natural Science Foundation of Guangdong Province (No. 2023A1515030236, 2026A1515012531), Shenzhen Science and Technology Program (Grant No. JCYJ20240813151418025, JCYJ20230807110809021).

References

1 A. Pei, P. Wang, S. Zhang, Q. Zhang, X. Jiang, Z. Chen, W. Zhou, Q. Qin, R. Liu, R. Du, *et al.*, Enhanced electrocatalytic biomass oxidation at low voltage by Ni2+-O-Pd interfaces, *Nat. Commun.*, 2024, **15**(1), 5899, DOI: 10.1038/s41467-024-50325-w.

2 Z. Yang, L. Chen, Y. Yin, C. Wei, Z. Xue and T. Mu, Weakened hydrogen bond connectivity promotes interfacial mass transfer for industrial level scalable biomass electrooxidation, *Energy Environ. Sci.*, 2024, **17**(22), 8801–8809, DOI: 10.1039/d4ee03482a.

3 Y. Li, H. Chen, F. Gao, Q. Chen, C. Li and J. He, The role of iron in Ni-Fe binary catalysts for electrochemical glycerol oxidation, *J. Colloid Interface Sci.*, 2025, **697**, 137913, DOI: 10.1016/j.jcis.2025.137913.

4 H. Liu, J. Yu, Y. Chen, J. Lee, W. Huang and W. Li, Cu-Based Bimetallic Catalysts for Electrocatalytic Oxidative Dehydrogenation of Furfural with Practical Rates, *ACS Appl. Mater. Interfaces*, 2023, **15**(31), 37477–37485, DOI: 10.1021/acsami.3c06783.

5 Y. Wang, H. Chen, Y. Tang and Y. Li, Research progress on 5-hydroxymethylfurfural electrocatalytic or photocatalytic oxidation coupling with hydrogen production, *Int. J. Hydrogen Energy*, 2025, **104**, 162–183, DOI: 10.1016/j.ijhydene.2024.09.442.

6 D. Chen, W. Li, J. Liu and L. Sun, Bio-inspired proton relay for promoting continuous 5-hydroxymethylfurfural electrooxidation in a flowing system, *Energy Environ. Sci.*, 2025, **18**(7), 3120, DOI: 10.1039/d4ee05745g.

7 J. Wu, J. Chen, T. Yu, Z. Zhai, Y. Zhu, X. Wu and S. Yin, Boosting Electrochemical Kinetics of NiCo2 via MoO2 Modification for Biomass Upgrading Assisted Hydrogen Evolution, *ACS Catal.*, 2023, **13**(20), 13257–13266, DOI: 10.1021/acscatal.3c03094.

8 H. Chen, C. Ding, Y. Li, L. Wang, C. Li and J. He, Bias-free photoelectrochemical system mediates hydrogen production and biomass conversion at high current density, *J. Environ. Chem. Eng.*, 2024, **12**(3), 112614, DOI: 10.1016/j.jece.2024.112614.

9 H. Chen, Y. Li, Z. Huang, L. Wang, C. Li and J. He, Robust Cu(0) active sites stabilized by high surface pH gradient for ultra-low-potential HMF oxidation, *J. Mater. Chem. A*, 2025, **13**(11), 8171–8179, DOI: 10.1039/d4ta08012b.

10 Y. Yang, X. Wu, M. Ahmad, F. Si, S. Chen, C. Liu, Y. Zhang, L. Wang, J. Zhang, J.-L. Luo, *et al.*, A Direct Formaldehyde Fuel Cell for CO2-Emission Free Co-generation of Electrical Energy and Valuable Chemical/Hydrogen, *Angew. Chem., Int. Ed.*, 2023, **62**(21), e202302950, DOI: 10.1002/anie.202302950.

11 N. C. Ramos and A. Holewinski, Recent advances in anodic hydrogen production: Electrochemical oxidative dehydrogenation of aldehydes to carboxylates, *Curr. Opin. Electrochem.*, 2024, **45**, 101484, DOI: 10.1016/j.coelec.2024.101484.

12 X. Li, L. Qi, W. Li, M. Wang, J. Xue, M. Chen and G. Wang, Electrooxidation of 5-hydroxymethylfurfural and electroreduction of nitrobenzene by hollow CoFeP cubes/rGO/Ni foam, *J. Mater. Chem. A*, 2025, **13**(29), 23525–23533, DOI: 10.1039/D5TA03005F.

13 Y. Li, H. Huang, M. Jiang, W. Xi, J. Duan, M. Ratova and D. Wu, Advancements in transition bimetal catalysts for electrochemical 5-hydroxymethylfurfural (HMF) oxidation, *J. Energy Chem.*, 2024, **98**, 24–46, DOI: 10.1016/j.jechem.2024.06.027.

14 X.-L. Liu, W. Zhong, Y.-F. Jin, T.-J. Wang, X. Xiao, P. Chen, Y. Chen and X. Ai, Pd-Pt bimetallene for the energy-saving electrochemical hydrogenation of 5-hydroxymethylfurfural, *Chin. J. Catal.*, 2025, **69**, 241–248, DOI: 10.1016/S1872-2067(24)60189-0.

15 P. Lu, B. Du, K. Liu, Z. Luo, A. Sikandaier, L. Diao, J. Sun, L. Jiang and Y. Zhu, Heterostructured In2O3/In2S3 hollow fibers enable efficient visible-light driven photocatalytic hydrogen production and 5-hydroxymethylfurfural oxidation, *Chin. J. Struct. Chem.*, 2024, **43**(8), 100361, DOI: 10.1016/j.cjsc.2024.100361.

16 I. R. Garduño-Ibarra, Z. Yan, S. A. Ebrahim, E. Baranova, J. González-Cobos, M. Prévot and P. Vernoux, Ni-Based Catalysts for 5-Hydroxymethylfurfural Electrooxidation Coupled with Hydrogen Production, *Chemelectrochem*, 2025, **12**(13), e202500067, DOI: 10.1002/celc.202500067.

17 J. Zhu, W. Wang, H. Wang, Y. Hou, X. Jiang, T. Xu, Z.-H. He, Y. Yang, Z.-T. Liu and B. Han, Revealing the electrochemical reconstruction behavior of Co(OH)2-NiSe for efficient the electrooxidation of 5-hydroxymethylfurfural, *Chem. Eng. J.*, 2025, **518**, 164632, DOI: 10.1016/j.cej.2025.164632.

18 J. Wang, J. Zhang and C. Chen, Electrochemical CO2RR to C2+products: A vision of dynamic surfaces of Cu-based catalysts, *Chin. J. Catal.*, 2025, **68**, 83–102, DOI: 10.1016/S1872-2067(24)60185-3.

19 M. Yang, Y. Li, C.-L. Dong, S. Li, L. Xu, W. Chen, J. Wu, Y. Lu, Y. Pan, Y. Wu, *et al.*, Correlating the Valence State with the Adsorption Behavior of a Cu-Based Electrocatalyst for Furfural Oxidation with Anodic Hydrogen Production Reaction, *Adv. Mater.*, 2023, **35**(39), 2304203, DOI: 10.1002/adma.202304203.

20 Y. Pan, Y. Li, C.-L. Dong, Y.-C. Huang, J. Wu, J. Shi, Y. Lu, M. Yang, S. Wang and Y. Zou, Unveiling the synergistic effect of multi-valence Cu species to promote formaldehyde oxidation for anodic hydrogen production, *Chem*, 2023, **9**(4), 963–977, DOI: 10.1016/j.chempr.2022.12.008.

21 Y. Jiang, H. Li, C. Chen, Y. Zheng and S.-Z. Qiao, Dynamic Cu0/Cu+ Interface Promotes Acidic CO2 Electroreduction, *ACS Catal.*, 2024, **14**(11), 8310–8316, DOI: 10.1021/acscatal.4c01516.

22 X. Cao, S. Ren, X. Zhang, Q. Fan, Q. Chen, J. Yang and J. Mao, Identification of Cu0/Cu+/Cu0 interface as superior active sites for CO2 electroreduction to C2+ in neutral condition, *Chem*, 2024, **10**(7), 2089, DOI: 10.1016/j.chempr.2024.02.014.

23 X. Yuan, S. Chen, D. Cheng, L. Li, W. Zhu, D. Zhong, Z.-J. Zhao, J. Li, T. Wang and J. Gong, Controllable Cu0-Cu+ Sites for Electrocatalytic Reduction of Carbon Dioxide, *Angew. Chem., Int. Ed.*, 2021, **60**(28), 15344–15347, DOI: 10.1002/anie.202105118.

24 Y. Lu, F. Yue, T. Liu, Y.-C. Huang, F. Fu, Y. Jing, H. Yang and C. Yang, Size-effect induced controllable Cu0-Cu+ sites for ampere-level nitrate electroreduction coupled with biomass upgrading, *Nat. Commun.*, 2025, **16**(1), 2392, DOI: 10.1038/s41467-025-57097-x.

25 H. Meng, Y. Yang, T. Shen, Z. Yin, L. Wang, W. Liu, P. Yin, Z. Ren, L. Zheng, J. Zhang, *et al.*, Designing Cu0-Cu+ dual sites for improved C-H bond fracture towards methanol steam reforming, *Nat. Commun.*, 2023, **14**(1), 7980, DOI: 10.1038/s41467-023-43679-0.

26 P. De Luna, R. Quintero-Bermudez, D. Cao-Thang, M. B. Ross, O. S. Bushuyev, P. Todorovic, T. Regier, S. O. Kelley, P. Yang and E. H. Sargent, Catalyst electro-redeposition controls morphology and oxidation state for selective carbon dioxide reduction, *Nat. Catal.*, 2018, **1**(2), 103–110, DOI: 10.1038/s41929-017-0018-9.

27 Q. Fan, P. Yan, F. Liu, Z. Xu, P. Liang, X. Cao, C. Ye, M. Liu, L. Zhao, S. Ren, *et al.*, Compressive strain in Cu catalysts: Enhancing generation of C2+ products in electrochemical CO2 reduction, *Sci. Bull.*, 2024, **69**(18), 2881–2891, DOI: 10.1016/j.scib.2024.06.031.

28 W.-J. Kang, Y. Feng, Z. Li, W.-Q. Yang, C.-Q. Cheng, Z.-Z. Shi, P.-F. Yin, G.-R. Shen, J. Yang, C.-K. Dong, *et al.*, Strain-Activated Copper Catalyst for pH-Universal Hydrogen Evolution Reaction, *Adv. Funct. Mater.*, 2022, **32**(18), 2112367, DOI: 10.1002/adfm.202112367.

29 Z. Hou, C. Cui, Y. Li, Y. Gao, D. Zhu, Y. Gu, G. Pan, Y. Zhu and T. Zhang, Lattice-Strain Engineering for Heterogenous Electrocatalytic Oxygen Evolution Reaction, *Adv. Mater.*, 2023, **35**(39), e2209876, DOI: 10.1002/adma.202209876.

30 W. Li, Y. Zhao, Y. Liu, M. Sun, G. I. N. Waterhouse, B. Huang, K. Zhang, T. Zhang and S. Lu, Exploiting Ru-Induced Lattice Strain in CoRu Nanoalloys for Robust Bifunctional Hydrogen Production, *Angew. Chem., Int. Ed.*, 2021, **60**(6), 3290–3298, DOI: 10.1002/anie.202013985.

31 T. He, W. Wang, F. Shi, X. Yang, X. Li, J. Wu, Y. Yin and M. Jin, Mastering the surface strain of platinum catalysts for efficient electrocatalysis, *NATURE*, 2021, **598**(7879), 76–81, DOI: 10.1038/s41586-021-03870-z.

32 W. Cheng, X. Zhao, H. Su, F. Tang, W. Che, H. Zhang and Q. Liu, Lattice-strained metal-organic-framework arrays for bifunctional oxygen electrocatalysis, *Nat. Energy*, 2019, **4**(2), 115–122, DOI: 10.1038/s41560-018-0308-8.

33 Q. Ji, Y. Kong, C. Wang, H. Tan, H. Duan, W. Hu, G. Li, Y. Lu, N. Li, Y. Wang, *et al.*, Lattice Strain Induced by Linker Scission in Metal-Organic Framework Nanosheets for Oxygen Evolution Reaction, *ACS Catal.*, 2020, **10**(10), 5691–5697, DOI: 10.1021/acscatal.0c00989.

34 W. Chen, Y. Shi, C. Liu, Z. Ren, Z. Huang, Z. Chen, X. Zhang, S. Liang, L. Xie, C. Lian, *et al.*, Restructuring the interfacial active sites to generalize the volcano curves for platinum-cobalt synergistic catalysis, *Nat. Commun.*, 2024, **15**(1), 8995, DOI: 10.1038/s41467-024-53474-0.

35 F. Shi, P. Tieu, H. Hu, J. Peng, W. Zhang, F. Li, P. Tao, C. Song, W. Shang, T. Deng, *et al.*, Direct in-situ imaging of electrochemical corrosion of Pd-Pt core-shell electrocatalysts, *Nat. Commun.*, 2024, **15**(1), 5084, DOI: 10.1038/s41467-024-49434-3.

36 A. Arcidiacono, C. Ruchlin, G. M. McLeod, D. Pattadar, S. Lindbom, A. J. Robb, S. Ayad, N. R. Dos Santos, I. V. Alabugin, S. S. Saavedra, *et al.*, Structural insights to metal ion linked multilayers on metal oxide surfaces via energy transfer and polarized ATR measurements, *J. Mater. Chem. A*, 2024, **12**(42), 28882–28891, DOI: 10.1039/d4ta05156d.

37 D. Gao, F. Scholten and B. R. Cuenya, Improved CO2 Electroreduction Performance on Plasma-Activated Cu Catalysts via Electrolyte Design: Halide Effect, *ACS Catal.*, 2017, **7**(8), 5112–5120, DOI: 10.1021/acscatal.7b01416.

38 D. Gao, I. Sinev, F. Scholten, R. M. Aran-Ais, N. J. Divins, K. Kvashnina, J. Timoshenko and B. Roldan Cuenya, Selective CO2 Electroreduction to Ethylene and Multicarbon Alcohols via Electrolyte-Driven Nanostructuring, *Angew. Chem., Int. Ed.*, 2019, **58**(47), 17047–17053, DOI: 10.1002/anie.201910155.

39 C. S. Chen, A. D. Handoko, J. H. Wan, L. Ma, D. Ren and B. S. Yeo, Stable and selective electrochemical reduction of carbon dioxide to ethylene on copper mesocrystals, *Catal. Sci. Technol.*, 2015, **5**(1), 161–168, DOI: 10.1039/c4cy00906a.

40 Z. Wei, J. Ding, X. Duan, G.-L. Chen, F.-Y. Wu, L. Zhang, X. Yang, Q. Zhang, Q. He, Z. Chen, *et al.*, Enhancing Selective Electrochemical CO2 Reduction by In Situ Constructing Tensile-Strained Cu Catalysts, *ACS Catal.*, 2023, **13**(7), 4711–4718, DOI: 10.1021/acscatal.3c00181.

41 Z. Zhai, D. Li, X. Lu, H. Cai, Q. Hu, H. Yang and C. He, Heteroatom-induced tensile strain in copper lattice boosts CO2 electroreduction toward multi-carbon products, *Carbon Energy*, 2024, **6**(12), e648, DOI: 10.1002/cey2.648.

42 J. Ma, W. Lee, J. H. Kim, J. Jeong, K.-m. Jo, S.-Y. Choi, S. Back and S. Y. Kim, Leveraging the Intermetal Distance in Dual-Atom Catalysts: Revealing Optimized Synergistic Interactions for CO2 Electroreduction, *ACS Nano*, 2025, **19**(19), 18698–18707, DOI: 10.1021/acsnano.5c03160.

43 H. Shi, L. Luo, C. Li, Y. Li, T. Zhang, Z. Liu, J. Cui, L. Gu, L. Zhang, Y. Hu, *et al.*, Stabilizing Cu+ Species in Cu2O/CuO Catalyst via Carbon Intermediate Confinement for Selective CO2RR, *Adv. Funct. Mater.*, 2024, **34**(11), 2310913, DOI: 10.1002/adfm.202310913.

44 C.-S. Tan, H.-Y. Chen, H.-S. Chen, S. Gwo and L.-J. Chen, Intermediates in the cation reactions in solution probed by an in situ surface enhanced Raman scattering method, *Sci. Rep.*, 2015, **5**(1), 13759, DOI: 10.1038/srep13759.

45 A. Hole, G. Tyagi, A. Sahu, R. Shaikh and C. M. Krishna, Exploration of Raman exfoliated cytology for oral and cervical cancers, *Vib. Spectrosc.*, 2018, **98**, 35–40, DOI: 10.1016/j.vibspec.2018.07.001.

46 M. J. Bushiri, C. J. Antony and M. Fleck, Raman and infrared spectral studies of [C(NH2)3]2MII(H2O)4(SO4)2, MII = Mn, Cd and VO, *J. Raman Spectrosc.*, 2008, **39**(3), 368–373, DOI: 10.1002/jrs.1828.

47 Z. Edis and S. H. Bloukh, Antimicrobial V-Shaped Copper(II) Pentaiodide: Insights to Bonding Pattern and Susceptibility, *Molecules*, 2022, **27**, 6437.

48 Q. Lei, L. Huang, J. Yin, B. Davaasuren, Y. Yuan, X. Dong, Z.-P. Wu, X. Wang, K. X. Yao, X. Lu, *et al.*, Structural evolution and strain generation of derived-Cu catalysts during CO2 electroreduction, *Nat. Commun.*, 2022, **13**(1), 4857, DOI: 10.1038/s41467-022-32601-9.

49 F. Ye, S. Zhang, Q. Cheng, Y. Long, D. Liu, R. Paul, Y. Fang, Y. Su, L. Qu, L. Dai, *et al.*, The role of oxygen-vacancy in bifunctional indium oxyhydroxide catalysts for electrochemical coupling of biomass valorization with CO2 conversion, *Nat. Commun.*, 2023, **14**(1), 2040, DOI: 10.1038/s41467-023-37679-3.

50 L. Zhao, Z. Lv, Y. Shi, S. Zhou, Y. Liu, J. Han, Q. Zhang, J. Lai and L. Wang, Simultaneous generation of furfuryl alcohol, formate, and H2 by co-electrolysis of furfuryl and HCHO over bifunctional CuAg bimetallic electrocatalysts at ultra-low voltage, *Energy Environ. Sci.*, 2024, **17**(2), 770–779, DOI: 10.1039/d3ee03761d.

51 X. Cao, Y. Tian, J. Ma, W. Guo, W. Cai and J. Zhang, Strong p-d Orbital Hybridization on Bismuth Nanosheets for High Performing CO2 Electroreduction, *Adv. Mater.*, 2024, **36**(6), 2309648, DOI: 10.1002/adma.202309648.

52 N. Li, P. Yan, Y. Tang, J. Wang, X.-Y. Yu and H. B. Wu, In-situ formation of ligand-stabilized bismuth nanosheets for efficient CO2 conversion, *Appl. Catal. B Environ.*, 2021, **297**, 120481, DOI: 10.1016/j.apcatb.2021.120481.

53 T. Kim, R. S. Assary, C. L. Marshall, D. J. Gosztola, L. A. Curtiss and P. C. Stair, Studies of the Raman spectra of cyclic and acyclic molecules: Combination and prediction spectrum methods, *Chem. Phys. Lett.*, 2012, **531**, 210–215, DOI: 10.1016/j.cplett.2012.02.002.

54 G. Fu, X. Kang, Y. Zhang, Y. Guo, Z. Li, J. Liu, L. Wang, J. Zhang, X.-Z. Fu and J.-L. Luo, Capturing critical gem-diol intermediates and hydride transfer for anodic hydrogen production from 5-hydroxymethylfurfural, *Nat. Commun.*, 2023, **14**(1), 8395, DOI: 10.1038/s41467-023-43704-2.

55 G. Allen and H. J. Bernstein, INTERNAL ROTATION: VIII. THE INFRARED AND RAMAN SPECTRA OF FURFURAL, *Can. J. Chem.*, 1955, **33**(6), 1055–1061, DOI: 10.1139/v55-121.

56 L. Banki, F. Billes, M. Ga'l, A. Grofcsik, G. Jalsovszky and L. Sztraka, Conformational Effect on CNDO Force Field of Furan-2-Aldehyde, *J. Mol. Struct.*, 1986, **142**, 351–354, DOI: 10.1016/0022-2860(86)85131-6.

57 H. Zang, Y. Zhao, C. Liu, H. Lu, N. Yu and B. Geng, Hierarchical Cavity Cu Nanostructures with Coordinative Microenvironment Engineering for pH-Universal Electrocatalytic CO2-to-C2+ Conversion, *Adv. Funct. Mater.*, 2025, **35**(35), 2504400, DOI: 10.1002/adfm.202504400.

58 H. Shi, Y. Liang, J. Hou, H. Wang, Z. Jia, J. Wu, F. Song, H. Yang and X. Guo, Boosting Solar-Driven CO2 Conversion to Ethanol via Single-Atom Catalyst with Defected Low-Coordination Cu-N2 Motif, *Angew. Chem., Int. Ed.*, 2024, **63**(31), e202404884, DOI: 10.1002/anie.202404884.